Superconductivity and Phase Stability of a High-Entropy $(NbTa)_{0.55}(HfTiZr)_{0.45}$ Alloy under High Pressures

Kallol Chakrabarty [a], Thomas Freeman [b], Greeshma C. Jose [a], Francisco J. canales [a], James L. Petri [a], Elizabeth C. Thompson [a,c], Wenli Bi [a], Abhinav Yadav [d], Vijaya Rangari [d], Yogesh K. Vohra [a*]

[a] Department of Physics, University of Alabama at Birmingham, AL 35294 USA
[b] Department of Physics, Middle Tennessee State University, TN 37132
[c] Department of Earth and Environmental Systems, The University of the South, Sewanee, Tennessee 37383, USA
[d] Department of Materials Science and Engineering, Tuskegee University, Alabama, 36088, USA

[*]Correspondence: ykvohra@uab.edu

Abstract

High-entropy alloys (HEAs) are a class of multi-element materials that exhibit unique structural and functional properties. This study reports on the synthesis and characterization of a superconducting HEA, $(NbTa)_{0.55}(HfTiZr)_{0.45}$ fabricated using the vacuum arc melting technique. Scanning electron microscopy (SEM) and energy-dispersive X-ray spectroscopy (EDS) were employed to analyze the material's morphology and composition. X-ray diffraction (XRD) analysis revealed a single-phase body-centered cubic (BCC) structure with a measured nanoindentation hardness of 6.4 GPa and Young's modulus of 132 GPa. This HEA superconductor was investigated by x-ray diffraction at Beamline 13BM-C, Advanced Photon Source and the BCC phase was stable to the highest pressure of 50 GPa. Superconductivity was characterized by four-probe resistivity measurements in a Quantum Design Physical Property Measurement System (PPMS), yielding a superconducting transition temperature (T_c) of 7.2 K at ambient pressure and reaching a maximum of 10.1 K at the highest applied pressure of 23.6 GPa. The combination of high structural stability enhanced superconducting performance under pressure, and superior mechanical properties highlights $(NbTa)_{0.55}(HfTiZr)_{0.45}$ as a promising superconductor under extreme environments.

Introduction

High-entropy alloys (HEAs) represent an emerging material class that has gathered significant attention in the global scientific community. These alloys are distinguished by their unique composition, consisting of five or more principal elements randomly occupying the crystallographic sites within their structure [1,2]. The remarkable properties of high-entropy alloys (HEAs) are fundamentally attributed to four core effects that distinguish them from conventional alloys [3,4]. First, the high entropy effect stabilizes solid solution phases by significantly reducing the Gibbs free energy. Gibb's free energy for this mixing can be expressed as $\Delta G_{mix} = \Delta H_{mix} - T\Delta S_{mix}$. Where ΔH_{mix} is the enthalpy of mixing, T is the absolute temperature, and ΔS_{mix} is the entropy of mixing. The expression of entropy of mixing is represented as $\Delta S_{mix} = \Delta S_{conf} = -R \sum_{i=1}^{n} x_i \ln x_i$ [1,5]. The presence of multiple principal elements significantly increases the configurational entropy or entropy of mixing. This elevated entropy often outweighs the enthalpy of mixing, resulting in a substantial reduction in the Gibbs free energy. Consequently, the Gibbs free energy becomes negative, favoring the stabilization of solid solution phases over more complex or ordered structures [3]. Second, the lattice distortion effect arises from the varying atomic sizes of the constituent elements, causing localized lattice strains. These distortions impede the movement of dislocations, thereby enhancing the mechanical strength and hardness of the material. Third, the sluggish diffusion effect reflects the reduced atomic mobility in HEAs due to their compositional complexity. This effect improves thermal stability, delays phase transformations, and contributes to the material's resistance to high-temperature degradation. Finally, the cocktail effect refers to the synergistic interactions among the multiple principal elements, leading to properties that surpass those predicted by the individual contributions of the constituent elements [6-10]. This effect allows for the optimization of HEAs for a wide range of applications by leveraging

the unique combinations of their components. These core effects strengthen the exceptional mechanical, thermal, and chemical performance of HEAs, making them a focus of intense research in condensed matter physics and materials science.

Superconductivity represents one of the most intriguing discoveries in HEAs. This breakthrough has opened new frontiers in understanding and developing materials with remarkable electronic properties. The first instance of superconductivity in an HEA was reported in the alloy $Ta_{34}Nb_{33}Hf_8Zr_{14}Ti_{11}$, as documented by Koželj et al [11]. This alloy was identified as a type-II superconductor, exhibiting a critical temperature of 7.3 K and an upper critical magnetic field of 82 kOe. The discovery of superconductivity in $Ta_{34}Nb_{33}Hf_8Zr_{14}Ti_{11}$ not only marked a significant milestone but also inspired extensive research for other high-entropy alloys with similar capabilities. This effort led to the identification of additional HEA superconductors, particularly those composed of transition metals. Notable examples include $Hf_{21}Nb_{25}Ti_{15}V_{15}Zr_{24}$ [12], which demonstrated promising superconducting properties, as well as $Ta_{1/6}Nb_{2/6}Hf_{1/61}Zr_{1/6}Ti_{1/6}$ and $Nb_{10+2x}Mo_{35-x}Ru_{35-x}Rh_{10}Pd_{10}$ (where $0 \leq x \leq 5$) [13,14]. Superconducting HEA thin films such as $(TaNb)_{1-x}(ZrHfTi)_x$ and $(TaNb)_{1-x}(ZrHfTi)_xMo_y$ has also been synthesized recently [15,16].

Pressure is a fundamental thermodynamic variable that can profoundly alter the structural, electronic, and magnetic properties of materials, often leading to the emergence of unexpected physical phenomena [17-21]. One of the most well-known effects of pressure in superconductors is the manipulation of critical transition temperatures. This has been extensively observed in copper-oxide (cuprate) superconductors and iron-based (pnictide) superconductors [22-25]. Additionally, pressure has been shown to induce superconductivity in systems where it was previously absent or suppressed. For example, in alkaline iron selenide and heavy fermion superconductors, pressure plays a crucial role in restoring superconducting order by modifying magnetic fluctuations and

electronic correlations [26,27]. Beyond these enhancements, pressure has also been instrumental in the discovery of entirely new superconducting states. A striking example is H_3S, a hydrogen sulfide compound that exhibits superconductivity at exceptionally high temperatures under megabar pressures [28-30]. Given the remarkable influence of pressure on superconducting materials, it is of great interest to investigate its effects on HEA superconductors. Understanding how superconducting HEAs respond to extreme pressure conditions may provide insight into their electronic interactions, stability, and potential for enhanced superconducting performance**.** In this study, we synthesized a superconducting HEA $(NbTa)_{0.55}(HfTiZr)_{0.45}$, characterized its structure and mechanical property, and explored the crystal structure and superconducting behaviors under high pressure, aiming to uncover new superconducting phenomena and broaden the scope of HEA-based superconductors in extreme environments.

Materials and Methods

The $(NbTa)_{0.55}(HfZrTi)_{0.45}$ sample was synthesized using MAM-1 vacuum arc melter. At first, high-purity metals (≥99.9%) were precisely weighed in stoichiometric proportions and compacted into a pellet using a hydraulic press. The pallet was placed on a water-cooled copper crucible on the arc melter to ensure rapid cooling and prevent reaction with the crucible material during the melt. To ensure uniform melting, the sample was flipped and re-melted four times, with each side exposed to the arc individually. This repeated melting cycle ensured a homogeneous composition throughout the bulk sample. After synthesis, smaller pieces of the sample were cleaved from the bulk structure using a diamond saw for further characterization. The crystal structure was obtained by a Panalytical Empyrean X-ray diffractometer (Copper $K_{\alpha 1}$, $\lambda = 1.54059$ Å).

A BX-90 diamond anvil cell (DAC) equipped with 300 μm culet diamond anvils was utilized for the high-pressure X-ray diffraction (XRD) experiments at the Beamline 13BM-C, Advanced Photon Source, Argonne National Laboratory. The X-ray wavelength was set to 0.4271 Å, and the beam focused to a 20 × 20 μm^2 size at the sample position. To increase the maximum 2θ angle, a cubic boron nitride (CBN) seat was used in the downstream facing the detector. A Re gasket with an initial thickness of 250 μm, pre-indented to a thickness of 45 μm, was used to create a sample chamber with a diameter of 130 μm drilled with electrical discharge machining. The sample dimensions were measured to be 80×35 μm^2 and 15 μm thick. Pressure was measured using ruby fluorescence [31]. Daphne oil 7575 was employed as the pressure-transmitting medium (PTM) to ensure quasi-hydrostatic conditions. An initial pressure of 3.7 GPa was applied prior to transportation to seal the pressure medium. The two-dimensional diffraction images were integrated in DIOPTAS software [32]. Le Bail refinements on the XRD data were performed in GSAS-II to extract the lattice parameter and volume [33].

The sample microstructures were analyzed using a JEOL JSM-7200F field emission scanning electron microscope (FESEM, JEOL USA, Peabody, MA) operated at an accelerating voltage of 15 kV. Mechanical properties such as nanoindentation hardness and modulus were measured using an Agilent Nano Indenter G200 with the continuous stiffness measurement (CSM) technique. A Berkovich diamond indenter tip with a nominal radius of 50 nm was employed for the tests. To ensure accuracy and reliability, the instrument was calibrated using a fused silica reference standard with a Young's modulus of 72±3GPa. Calibration indentations were performed on the silica standard before and after testing the sample. The consistent Young's modulus values obtained during these calibrations confirmed the stability of the indenter tip geometry, ensuring precise and reproducible hardness and modulus measurements.

Electrical resistance measurements of $(NbTa)_{0.55}(HfTiZr)_{0.45}$ sample was performed using the Quantum Design Physical Property Measurement System (PPMS-DynaCool) with the Electrical Transport Option (ETO) for four-probe resistance measurements. In ambient pressure resistance measurement, four Pt wires of 50 μm diameter were attached to a thin plate-like sample using silver paint. The high-pressure environment was achieved using a Be-Cu alloy DAC with 500 μm culet diamond anvils. The resistance measurements were conducted with an AC current of 0.5 mA at 18.3 Hz. A stainless-steel gasket, initially 250 μm thick, was pre-compressed to 72 μm, and a 176 μm diameter hole was drilled at its center. The gasket was then insulated with a mixture of cubic boron nitride and epoxy, and a 100 μm diameter sample chamber was created. Platinum foils shaped into thin wedges served as electrodes. The $(NbTa)_{0.55}(HfTiZr)_{0.45}$ sample was positioned at the center of the sample chamber in contact with four probes. Experiments were conducted under non-hydrostatic conditions, with pressure measured at room temperature using ruby fluorescence methods [31]. Pressure measurements were taken both before and after resistance measurements at low temperatures, and no pressure change was observed.

Results

Energy Dispersive X-ray Analysis

Energy dispersive X-ray analysis was carried out to measure the elemental composition of the HEA sample. From Figure 1 we can clearly see that there is no elemental segregation, and all the elements were uniformly distributed throughout the sample.

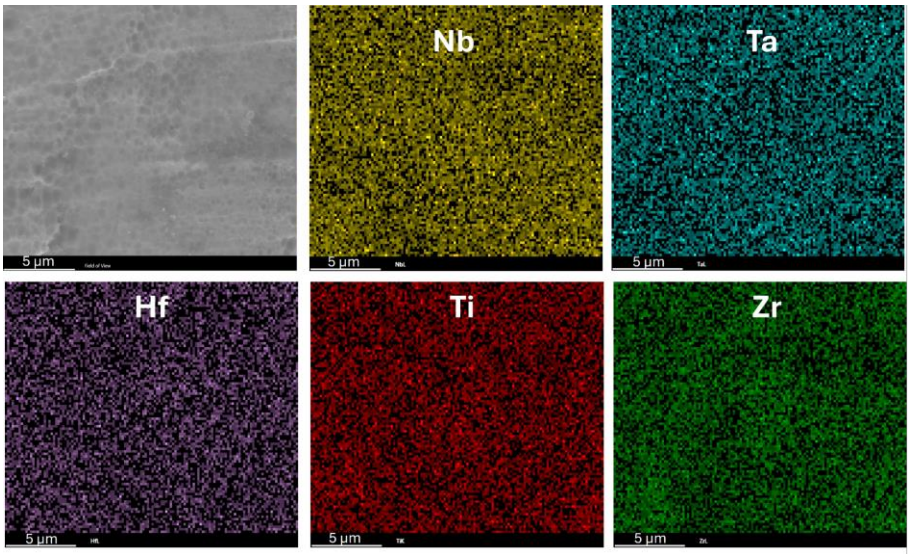

Element	Atomic %	Error %
Nb	24	6.6
Ta	31	3.9
Hf	16	4.5
Ti	13	4.5
Zr	16	7.4

Figure 1: SEM micrograph (top left image) and EDS elemental mapping (other images) of the $(NbTa)_{0.55}(HfTiZr)_{0.45}$ sample showing the uniform distribution of constituent elements in the alloy. EDS Atomic % is also presented here.

X-ray Diffraction

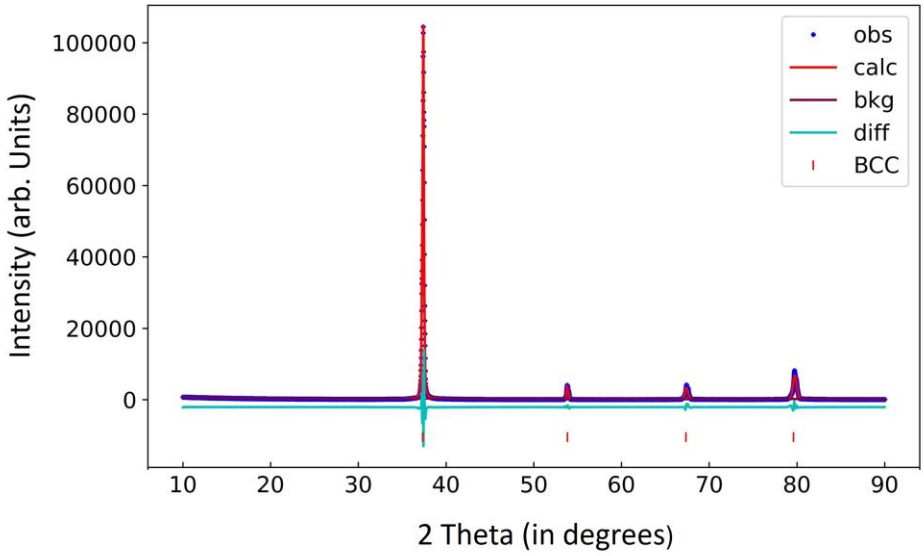

Figure 2: X-ray diffraction of synthesized $(NbTa)_{0.55}(HfTiZr)_{0.45}$ sample showing a single-phase BCC crystal structure.

Fig. 2 represents the XRD of the synthesized HEA sample indicating a body-centered cubic (BCC) crystal structure (space group *Im*-3*m*). No reflections corresponding to secondary phases

were observed. The reflections from the two theta positions (in degrees) at 37.3, 53.8, 67.3, and 79.6 represents the (110), (200), (211), and (220) crystal planes of the BCC crystal structure, respectively. The data provides no evidence of elemental ordering or the formation of lower-symmetry structures, reinforcing the conclusion that the alloy maintains a disordered solid solution characteristic of high-entropy alloys. The lattice parameter was obtained by Rietveld refinement. According to the analysis, the lattice parameter of the synthesized sample was 3.4 Å. The unit cell parameter for the observed BCC HEA exhibits variation within the solid solution, ranging from approximately 3.33 Å to 3.43 Å. [11,34,35]

High Pressure Synchrotron X-ray Diffraction

To investigate the structural stability of $(NbTa)_{0.55}(HfTiZr)_{0.45}$ under high pressure XRD data were collected under compression to 50 GPa. As shown in Figure 3, the diffraction peaks exhibit a continuous shift toward the higher angle with increasing pressure, indicative of the stability of the BCC crystal structure throughout the investigated pressure range. This is further supported by the pressure–volume relationship presented in Figure 4. A fit to the equation of state data was attempted using a third-order Birch-Murnaghan equation of state [36]. From the fitting, the zero-pressure bulk modulus (B_0) was determined to be 176 GPa, with a B' of 2.34. The zero-pressure unit cell volume (V_0) was 38.64 $Å^3$, consistent with the volume obtained at ambient pressure using the in-house XRD.

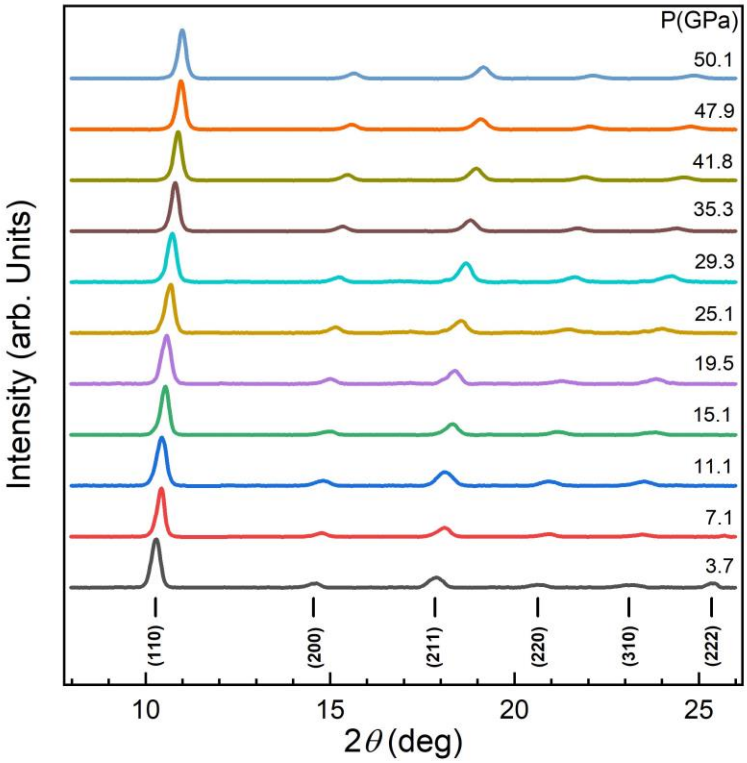

Figure 3: XRD patterns at various pressures from 3.7 GPa to 50.1 GPa. The synchrotron X-ray wavelength is 0.4271 Å. The XRD data was collected at ambient temperature, and pressure was measured by ruby fluorescence.

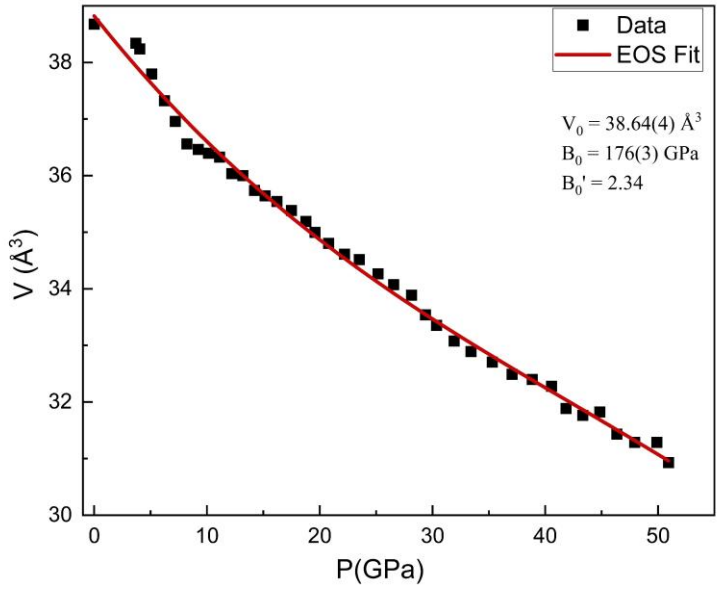

Figure 4: Pressure dependence of the unit cell volume. The red curve shows the fitting by third-order Birch–Murnaghan equation of state (BM EOS). B_0 was determined to be 176 GPa, with a V_0 of 38.6467 Å^3. The scatter in the data below 10 GPa is due to materials strength effects in a non-hydrostatic compression.

Electrical Resistance Measurements

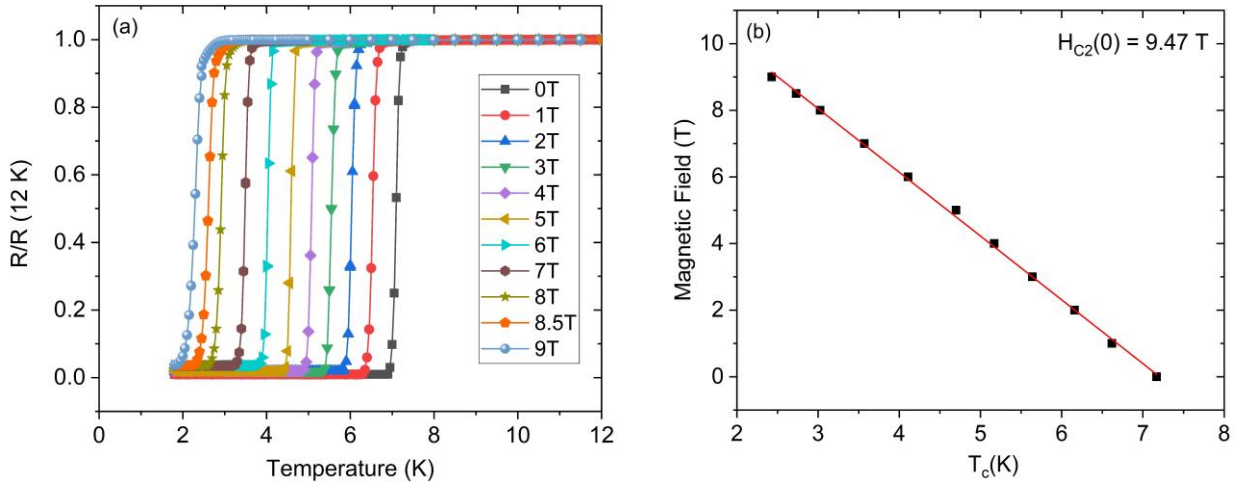

Figure 5: (a) Superconducting transition under various magnetic fields (b) Linear fit to find H_{c2} using WHH model at ambient pressure.

The superconductivity of $(NbTa)_{0.55}(HfTiZr)_{0.45}$ was examined using the four-probe method under a magnetic field ranging from 0T to 9T. Figure 5(a) illustrates the normalized resistance as a function of temperature for various applied magnetic fields. A sharp drop in resistance to zero signifies the onset of superconductivity, a hallmark of the material's transition into the superconducting state. The superconducting critical temperature (T_c) was determined as the temperature corresponding to 90% of the resistance drop from its normal-state value. As the applied magnetic field increases, the T_c systematically decreases. This phenomenon reflects the suppression of superconductivity under external magnetic fields, attributed to breaking Cooper pairs or modifications to the superconducting order parameter. The upper critical field H_{c2} can be derived from the slope of the critical temperature versus the magnetic field curve using the Werthimer-Helfand-Hohenberg (WHH) model [37],

$$H_{c2} = -0.69T_c(0)\left(\frac{dH}{dT}\right)_{T=T_c}$$

Where $\left(\frac{dH}{dT}\right)_{T=T_c}$ is the slope of the critical temperature versus the magnetic field curve and $T_c(0)$ is the critical temperature (T_c) without any magnetic field. From Fig. 5(b), the slope of the curve is measured and used in the WHH model to calculate the upper critical field of $(NbTa)_{0.55}(HfTiZr)_{0.45}$ sample as 9.47 T.

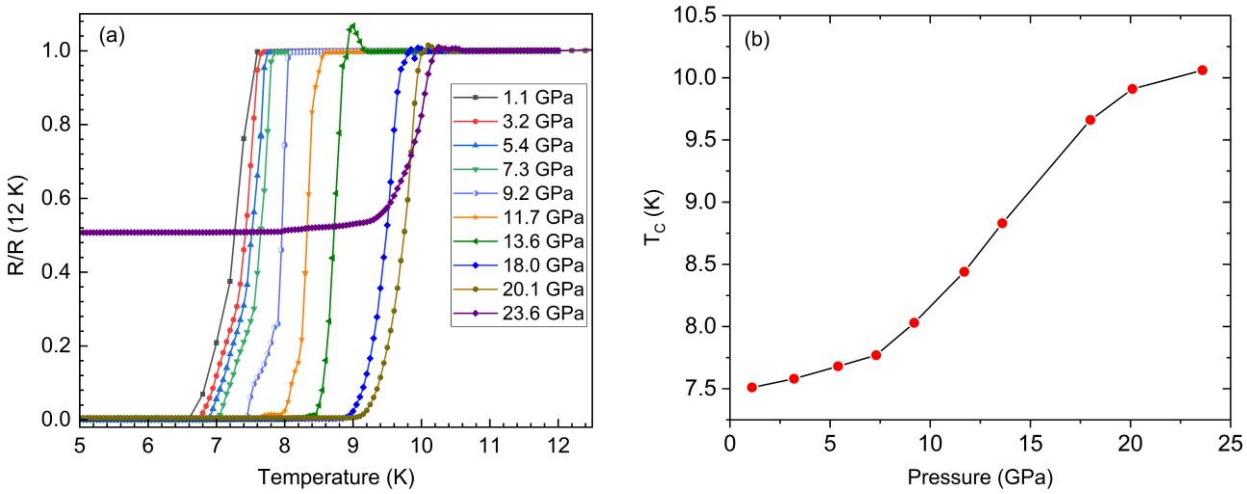

Figure 6: (a) Superconducting transition at pressures from 1.1 GPa to 23.6 GPa. (b) Pressure dependence of T_c

The effect of high pressure on superconducting $(NbTa)_{0.55}(HfTiZr)_{0.45}$ was investigated using the four-probe method under pressures ranging from 1.1 GPa to 23.6 GPa. The Figure 6(a) displays the normalized resistance as a function of temperature, with the drop to zero resistance marking the onset of superconductivity. The superconducting T_c was determined at 90% of the onset of the transition. An increase in pressure leads to a continuous rise in T_c. At 23.6 GPa, although the resistance does not drop completely to zero, likely due to shorting of the sample to the metallic gasket. The superconducting transition is clearly visible and supported by high-field measurements. Figure 6(b) further illustrates the continuous increase in T_c as a function of pressure, reinforcing the trend of pressure-enhanced superconductivity in this material.

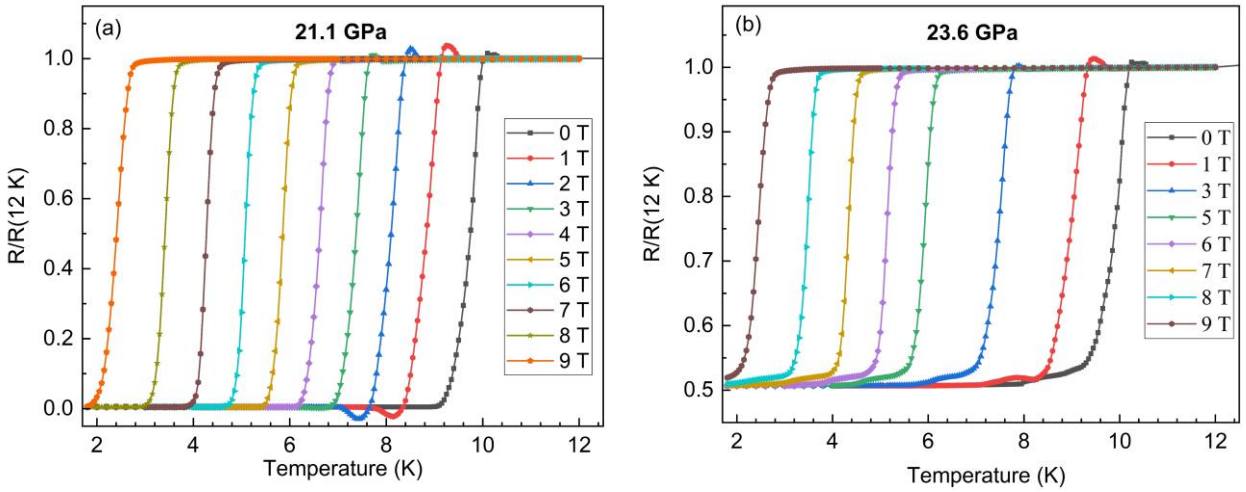

Figure 7: Normalized resistance at different temperatures under different applied magnetic fields for (a) 21.1 GPa and (b) 23.6 GPa.

Figure 7(a) and 7(b) represents the temperature dependence of normalized resistance as a function of an applied perpendicular magnetic field, up to 9 T, within the temperature range of 2–12 K for two pressures: 21.1 GPa and 23.6 GPa respectively. The normal-state resistance remains unaffected by the magnetic field. However, as the field strength increases, T_c shifts to lower values, confirming the presence of superconductivity.

The T_c at different applied magnetic fields for pressures of 21.1 GPa and 23.6 GPa can be determined from Figure 7(a) and Figure 7(b), respectively. Using this data, the dependence of T_c on the magnetic field can be plotted for each pressure, as shown in Figure 8(a) for 21.1 GPa and Fig. 8(b) for 23.6 GPa. From these plots, the slope of the T_c vs. magnetic field curves provides a key parameter for estimating the upper critical field at each pressure. Based on the WHH model, the upper critical field values were calculated to be 8.85 T for 21.1 GPa and 8.51 T for 23.6 GPa.

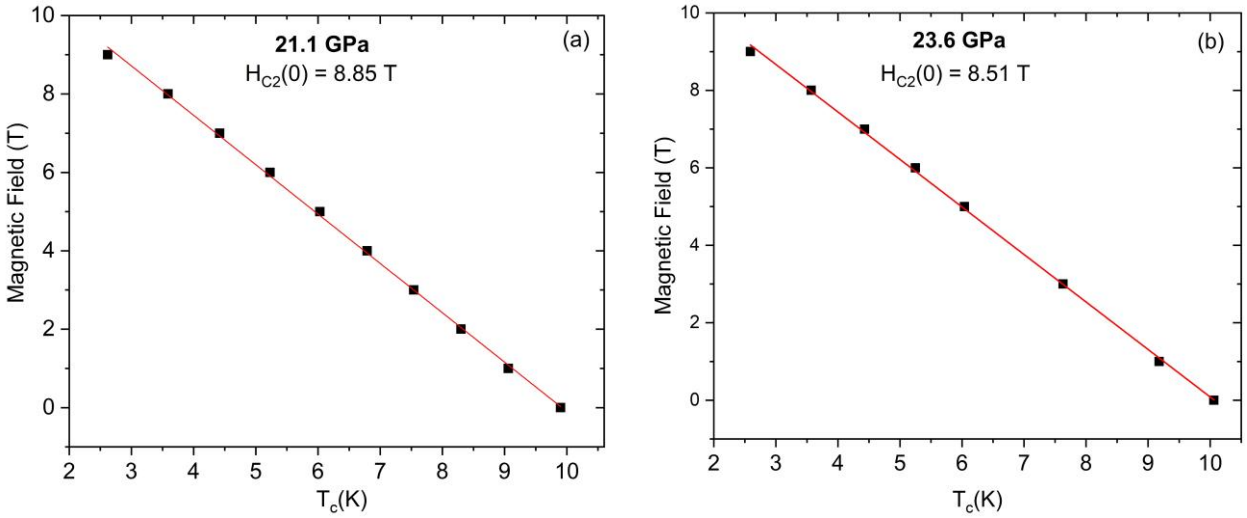

Figure 8: (a) Linear fit to find H_{c2} using WHH model for 21.1 GPa and (b) 23.6 GPa.

Nanoindentation Hardness and Modulus:

All nanoindentation tests, including those performed on silica for calibration, were conducted using the continuous stiffness measurement (CSM) method with a maximum penetration depth of 1000 nm. Figure 9(a) presents the variation of hardness as a function of displacement into the surface, as determined by the CSM technique. Hardness values were calculated within a depth range of 100–900 nm. Across this range, the hardness exhibited minimal variation, yielding an average value of 6.3 GPa with a standard deviation of 0.7 GPa. The low variability indicates excellent measurement reliability and uniform mechanical properties throughout the sample depth. Similarly, Figure 9(b) displays the variation of Young's modulus as a function of displacement into the surface. Modulus values were also computed within the 100–900 nm range. Across this depth range, the modulus remained consistent, with a mean value of 132.3 GPa and a standard deviation of 9 GPa. This consistency in modulus across the depth range highlights the homogeneity of the sample's elastic properties. Figure 9(c) presents load-displacement curves obtained from 25 indentations performed across various regions of the HEA

sample. The nearly identical behavior of these curves across all test points demonstrates the sample's structural and mechanical uniformity. The relative contributions of elastic and plastic deformation can be assessed by analyzing the ultimate unloading depth of these load-displacement curves. This comprehensive analysis confirms the consistency of the mechanical properties across the sample and highlights the robustness of the CSM method for characterizing complex materials.

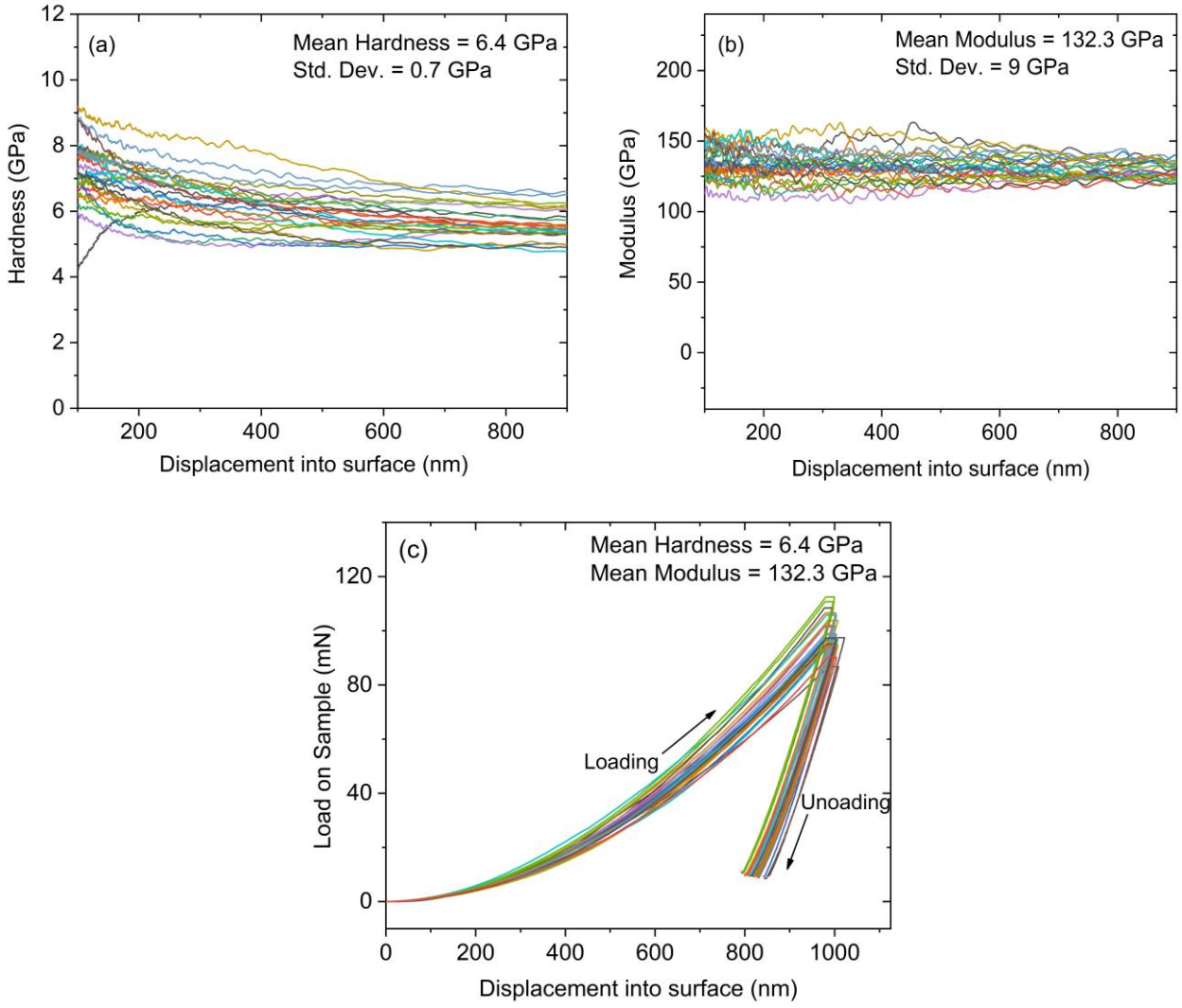

Figure 9: (a) Continuous stiffness measurement hardness data from 25 indents, displaying the mean hardness value of 6.4 GPa. (b) Continuous stiffness measurement modulus data from 25 indents shows the mean modulus value of 132.3 GPa. (c) The nanoindentation load-displacement curve was obtained from 25 indents, revealing a mean hardness of 6.4 GPa at a depth of 1000 nm.

Discussion

The superconducting and structural properties of the high-entropy alloy $(NbTa)_{0.55}(HfTiZr)_{0.45}$ were systematically investigated under high-pressure conditions. The experimental findings confirm the stability of this material's BCC structure up to 50 GPa, as observed through high XRD measurements. In contrast, many conventional alloys undergo phase changes or chemical segregation at significantly lower pressures [38,39]. The retention of the BCC phase, even as the unit cell volume steadily decreases, underscores the synergistic influence of refractory elements (Nb, Ta, Hf, Zr, Ti) and high configurational entropy [10]. The stability of the BCC phase under extreme conditions highlights the alloy's resilience, making it a promising candidate for superconducting applications in high-pressure environments.

The pressure-dependent superconducting behavior of $(NbTa)_{0.55}(HfTiZr)_{0.45}$ provides valuable insight into its electronic properties. The material exhibits a T_c of 7.2 K at ambient pressure. However, with increasing pressure, T_c rises steadily, reaching a maximum of 10.1 K at 23.6 GPa. Pressure can modify superconducting properties through changes in the density of states at the Fermi level, phonon frequencies, and electron-phonon coupling constants [40,41]. In particular, the absence of any pressure-driven phase transition within the studied range implies that the observed T_c enhancement arises primarily from electronic and lattice dynamical effects rather than changes in crystal symmetry. The observed increase in T_c is likely attributed to an increase in the Debye temperature, which enhances electron-phonon coupling [22,24]. The increase in Debye temperature under compression is a well-known factor that strengthens electron-phonon interactions, thereby promoting superconductivity [21,25]. Pressure typically increases phonon frequencies (reflected in a higher Debye temperature), thereby enhancing the electron-phonon coupling constant λ. Since λ features prominently in the Allen-Dynes equation for T_c, its increase

under compression can boost superconducting properties [42]. Furthermore, the upper critical field (H_{c2}) evaluated by the Werthamer-Helfand-Hohenberg (WHH) model (9.5 T at ambient pressure) suggests that this alloy can sustain superconductivity in relatively high magnetic fields. The suppression of T_c with increasing magnetic field aligns with typical type-II superconducting behavior, where the formation of vortex states governs the superconducting state's stability [27]. This characteristic suggests that $(NbTa)_{0.55}(HfTiZr)_{0.45}$ follows a conventional phonon-mediated superconducting mechanism despite its compositionally complex nature. The WHH model also provided estimates of the H_{c2} with applied pressure. This H_{c2} under compression corroborates the notion of strengthened superconductivity since type-II superconductors with more robust pairing correlations typically tolerate higher magnetic fields before reverting to a normal state [37]. Notably, this attribute is crucial for technological uses in high-field magnets and cryogenic systems, where materials often confront intense magnetic and mechanical stresses.

Table 1 : Superconducting parameters of some of the HEA and High entropy ceramics

Composition	**Tc (K)**	**Highest Tc (K) (at applied pressure)**	**$\mu_0 H_{c2}(0)$ (T) (at ambient pressure)**	**References**
$AgInSnPbBiTe_5$	1.8	5.3 (35.1GPa)	Not calculated	[43]
$(Ti_{0.2}Zr_{0.2}Nb_{0.2}Hf_{0.2}Ta_{0.2})C$	2.35	2.15 (80 GPa)	0.51	[44]
$Ti_{0.2}Zr_{0.2}Nb_{0.2}Mo_{0.2}Ta_{0.2}C_1$	4.0	4.45 (15.8 GPa)	2.5	[45]
$(NbTa)_{0.45}(ZrHfTi)_{0.55}$	6.1	Not calculated	4.92	[46]
$(NbTa)_{0.67}(HfTiZr)_{0.33}$	7.7	10 (60 GPa)	8	[21]
TaNbHfZr	8.1	15.3 (71.6 GPa)	16.3	[47]
$(NbTa)_{0.55}(HfTiZr)_{0.45}$	7.2	10.1 (23.6 GPa)	9.47	This work

As shown in the table 1, the high entropy carbides $Ti_{0.2}Zr_{0.2}Nb_{0.2}Mo_{0.2}T_{0.2}C_1$ and $(Ti_{0.2}Zr_{0.2}Nb_{0.2}Hf_{0.2}Ta_{0.2})C$ show relatively lower T_c at ambient pressure, but also undergo modest shifts under compression. HEA superconductors exhibit ambient-pressure T_c values typically ranging from about 2 K to 8 K, while applied pressures can significantly enhance their T_c. Notably, TaNbHfZr attains the highest reported T_c of 8.1 K at ambient pressure and 15.3 K at 71.6 GPa, accompanied by a large upper critical field of 16.3 T. Applied high pressure can notably increase T_c, as demonstrated by TaNbHfZr, which attains 15.3 K at 71.6 GPa, the highest transition temperature among these examples. Similarly, $(NbTa)_{0.67}(HfTiZr)_{0.33}$ approaches 10 K at 60 GPa. Our synthesized sample $(NbTa)_{0.55}(HfTiZr)_{0.45}$ exhibits Tc =7.2K and increases to 10.1K under 23.6 GPa, and we believe the T_c would continue to rise at higher pressures; however, due to technical issues during the experiment, we were unable to proceed beyond 23.6 GPa. Such pressure dependence suggests strong electron-phonon coupling that can be tuned by modifying the lattice parameters.

The main rationale for synthesizing a $(NbTa)_{0.55}(HfTiZr)_{0.45}$ was to develop a superconducting $(NbTa)_{1-x}(HfTiZr)_x$ with a higher upper critical field (Hc_2). According to the literature, the Hc_2 of the $(NbTa)_{1-x}(HfTiZr)_x$ increases with increasing x. The Hc_2 of the $(NbTa)_{0.7}(HfTiZr)_{0.3}$ sample is 6.67 T with a T_c of 8.03 K [34]. Our primary objective was to synthesize a sample with an enhanced Hc_2 while minimizing the reduction in the superconducting T_c. In our study, we successfully achieved a substantial increase in the Hc_2, reaching 9.47 T, which marks a significant 41% improvement compared to $(NbTa)_{0.7}(HfTiZr)_{0.3}$. Although this enhancement came at the expense of a slight decrease in T_c, the observed transition temperature of our sample remained relatively high at 7.2 K, reflecting only a modest 10% reduction. This trade-

off underscores that our synthesis approach successfully improves the material's performance in high-field applications while maintaining robust superconductivity.

Beyond its superconducting characteristics, $(NbTa)_{0.55}(HfZrTi)_{0.45}$ displays very good mechanical strength, with a hardness of 6.4 GPa and a Young's modulus of 132.3 GPa. These results underscore the advantage of employing refractory elements known for their high melting points and strong bonding in high-entropy alloys [1,39] . These results suggest that the material can withstand high-pressure conditions without significant structural degradation, further reinforcing its potential for applications in extreme environments. Compared to conventional metallic superconductors (e.g., niobium or Nb-Ti alloys), which typically exhibit lower hardness (often <4 GPa), this alloy provides a unique balance of mechanical and superconducting properties [48,49]. The uniformity in nanoindentation responses across different regions of the sample points to a homogeneous distribution of the constituent elements, consistent with prior findings that illustrate sluggish diffusion and high solubility in HEAs [38,39].

The hardness values of HEAs spans a broad range. For example, the hardness values (1.1-8.8 GPa) of a few common HEAs have been listed in Table 2. The measured hardness of 6.4 GPa for the $(NbTa)_{0.55}(HfTiZr)_{0.45}$ alloy in this study falls within the upper range commonly observed for HEAs.

Table 2: Hardness values of the most studied HEAs

Composition	**Hardness (GPa)**	**References**
$FeNiCrCoAl_{0.25}$	1.1	[50]
CoCrFeMnNi	1.4	[51]

TiZrHfNbTa	3.5	[52]
$FeNiCrCoAl_{0.75}$	3.8	[50]
AlCrFeNiCoCu	5.7	[53]
$Al_{0.5}CrFeNiCo_{0.3}C_{0.2}$	6.1	[54]
$FeNiCrCo_{0.3}Al_{0.7}$	6.1	[55]
$AlCoCrFeNiV_1$	6.4	[56]
CoCrFeMnNiV	6.4	[51]
CoCrFeNiMnAl	6.5	[57]
$Al_{0.6}CoNiFeTi_{0.4}$	6.9	[58]
$AlCoCrFeNi_{2.1}$	7.2	[59]
$AlCoNiFeCrNb_{0.5}$	7.3	[60]
CuNiCoZnAlTi	8.8	[61]

The synergy between mechanical strength and pressure-enhanced superconductivity underscores the potential of $(NbTa)_{0.55}(HfTiZr)_{0.45}$ where materials are subjected to severe operating conditions. For instance, high-field magnets for fusion reactors or space exploration applications require superconductors that can withstand both cryogenic temperatures and mechanical loads [62]. Maintaining (and even enhancing) superconducting properties at elevated pressures could also be advantageous in specialized instrumentation. The mechanical properties and enhanced superconductivity under pressure make this $(NbTa)_{0.55}(HfTiZr)_{0.45}$ high-entropy alloy a compelling material for technological applications requiring mechanical stability and superconducting functionality.

The interplay between pressure and superconductivity in this alloy is crucial for understanding its behavior's underlying mechanisms. The increasing T_c with pressure suggests tuning the electronic band structure through external compression can optimize superconducting properties. Further theoretical modeling and spectroscopic studies, such as high-pressure tunneling spectroscopy or neutron scattering, would be highly beneficial for elucidating the detailed changes in the electronic states and phonon contributions under compression. Overall, these results align with the broader trend in high-entropy materials research, where compositionally complex alloys are increasingly recognized for their novel phase stability, mechanical resilience, and tunable physical properties [10,38,39].

Conclusion

In summary, $(NbTa)_{0.55}(HfZrTi)_{0.45}$ alloy stands out as a robust high-entropy alloy combining exceptional structural stability, enhanced superconductivity, and superior mechanical performance. Specifically, the material retains its BCC phase up to 50 GPa with no evidence of phase transitions, exhibits a pressure-induced increase in superconducting transition temperature (T_c) reaching 10.1 K, and demonstrates a hardness of approximately 6.4 GPa along with a Young's modulus of about 132.3 GPa. The upper critical field observed under compression aligns with a phonon-mediated superconducting mechanism that benefits from external pressure. These attributes collectively underscore the alloy's strong potential for demanding applications in high-pressure technologies, superconducting magnets, and quantum devices.

Acknowledgments

This material is based upon work supported by the National Science Foundation (NSF) under Grant No. DMR-2310526. The Physical Properties Measurements System (PPMS) employed in this study was acquired under NSF MRI Grant No. 2215143. Portions of this work were performed at GeoSoilEnviroCARS (Sector 13), Advanced Photon Source, Argonne National Laboratory. GeoSoilEnviroCARS is supported by the NSF – Earth Sciences via SEES: Synchrotron Earth and Environmental Science (EAR–2223273). The Advanced Photon Source is a U.S. Department of Energy (DOE) Office of Science User Facility operated for the DOE Office of Science by Argonne National Laboratory under Contract No. DE-AC02-06CH11357. Thomas Freeman acknowledges support from the NSF REU-site under Grant No. DMR-2148897. G.C. Jose, J.L. Petri, E.C. Thompson, and W. Bi acknowledge the support from NSF CAREER Award No. DMR-2045760.

DATA AVAILABILITY

The data that support the findings of this study are available from the corresponding author upon reasonable request.

References

[1] S. A. Krishna, N. Noble, N. Radhika, and B. Saleh, Journal of Manufacturing Processes **109,** 583 (2024).

[2] D. Li, P. K. Liaw, L. Xie, Y. Zhang, and W. Wang, Journal of Materials Science & Technology **186,** 219 (2024).

[3] Y. F. Ye, Q. Wang, J. Lu, C. T. Liu, and Y. Yang, Materials Today **19,** 349 (2016).

[4] L. Sun and R. J. Cava, Physical Review Materials **3** (2019).

[5] S. Kumar, Surface and Coatings Technology **477,** 130327 (2024).

[6] B. Yin, F. Maresca, and W. A. Curtin, Acta Materialia **188,** 486 (2020).

[7] J. Dąbrowa, G. Cieślak, M. Stygar, K. Mroczka, K. Berent, T. Kulik, and M. Danielewski, Intermetallics **84,** 52 (2017).

[8] J. Lu, Y. Chen, H. Zhang, L. Li, L. Fu, X. Zhao, F. Guo, and P. Xiao, Corrosion Science **170,** 108691 (2020).

[9] M. J. Yao, K. G. Pradeep, C. C. Tasan, and D. Raabe, Scripta Materialia **72-73,** 5 (2014).

[10] D. B. Miracle and O. N. Senkov, Acta Materialia **122,** 448 (2017).

[11] P. Kozelj, S. Vrtnik, A. Jelen, S. Jazbec, Z. Jaglicic, S. Maiti, M. Feuerbacher, W. Steurer, and J. Dolinsek, Phys Rev Lett **113,** 107001 (2014).

[12] N. Ishizu and J. Kitagawa, Results in Physics **13,** 102275 (2019).

[13] G. Kim, M.-H. Lee, J. H. Yun, P. Rawat, S.-G. Jung, W. Choi, T.-S. You, S. J. Kim, and J.-S. Rhyee, Acta Materialia **186,** 250 (2020).

[14] B. Liu, J. Wu, Y. Cui, Q. Zhu, G. Xiao, S. Wu, G. Cao, and Z. Ren, Scripta Materialia **182,** 109 (2020).

[15] X. Zhang, R. Shu, H. Liu, A. Elsukova, P. O. Å. Persson, A. Schilling, F. O. von Rohr, and P. Eklund, Communications Physics **5** (2022).

[16] X. Zhang, P. Eklund, and R. Shu, Applied Physics Letters **123** (2023).

[17] R. J. Hemley and N. W. Ashcroft, Physics Today **51,** 26 (1998).

[18] H.-K. Mao, B. Chen, J. Chen, K. Li, J.-F. Lin, W. Yang, and H. Zheng, Matter and Radiation at Extremes **1,** 59 (2016).

[19] R. P. Dias and I. F. Silvera, Science **355,** 715 (2017).

[20] Y. Ma, M. Eremets, A. R. Oganov, Y. Xie, I. Trojan, S. Medvedev, A. O. Lyakhov, M. Valle, and V. Prakapenka, Nature **458,** 182 (2009).

[21] J. Guo, H. Wang, F. von Rohr, Z. Wang, S. Cai, Y. Zhou, K. Yang, A. Li, S. Jiang, Q. Wu, R. J. Cava, and L. Sun, Proc Natl Acad Sci U S A **114,** 13144 (2017).

[22] C. W. Chu, L. Gao, F. Chen, Z. J. Huang, R. L. Meng, and Y. Y. Xue, Nature **365,** 323 (1993).

[23] X. J. Chen, V. V. Struzhkin, Y. Yu, A. F. Goncharov, C. T. Lin, H. K. Mao, and R. J. Hemley, Nature **466,** 950 (2010).

[24] H. Takahashi, K. Igawa, K. Arii, Y. Kamihara, M. Hirano, and H. Hosono, Nature **453,** 376 (2008).

[25] S. Medvedev, T. M. McQueen, I. A. Troyan, T. Palasyuk, M. I. Eremets, R. J. Cava, S. Naghavi, F. Casper, V. Ksenofontov, G. Wortmann, and C. Felser, Nat Mater **8,** 630 (2009).

[26] L. Sun, X. J. Chen, J. Guo, P. Gao, Q. Z. Huang, H. Wang, M. Fang, X. Chen, G. Chen, Q. Wu, C. Zhang, D. Gu, X. Dong, L. Wang, K. Yang, A. Li, X. Dai, H. K. Mao, and Z. Zhao, Nature **483,** 67 (2012).

[27] H. Q. Yuan, F. M. Grosche, M. Deppe, C. Geibel, G. Sparn, and F. Steglich, Science **302,** 2104 (2003).

[28] D. Duan, Y. Liu, F. Tian, D. Li, X. Huang, Z. Zhao, H. Yu, B. Liu, W. Tian, and T. Cui, Sci Rep **4,** 6968 (2014).

[29] A. P. Drozdov, M. I. Eremets, I. A. Troyan, V. Ksenofontov, and S. I. Shylin, Nature **525,** 73 (2015).

[30] I. Troyan, A. Gavriliuk, R. Ruffer, A. Chumakov, A. Mironovich, I. Lyubutin, D. Perekalin, A. P. Drozdov, and M. I. Eremets, Science **351,** 1303 (2016).

[31] G. Shen, Y. Wang, A. Dewaele, C. Wu, D. E. Fratanduono, J. Eggert, S. Klotz, K. F. Dziubek, P. Loubeyre, O. V. Fat'yanov, P. D. Asimow, T. Mashimo, and R. M. M. Wentzcovitch, High Pressure Research **40,** 299 (2020).

[32] C. Prescher and V. B. Prakapenka, High Pressure Research **35,** 223 (2015).

[33] B. H. Toby and R. B. Von Dreele, Journal of Applied Crystallography **46,** 544 (2013).

[34] F. von Rohr, M. J. Winiarski, J. Tao, T. Klimczuk, and R. J. Cava, Proc Natl Acad Sci U S A **113,** E7144 (2016).

[35] O. N. Senkov, J. M. Scott, S. V. Senkova, D. B. Miracle, and C. F. Woodward, Journal of Alloys and Compounds **509,** 6043 (2011).

[36] F. Birch, Journal of Geophysical Research: Solid Earth **83,** 1257 (2012).

[37] N. R. Werthamer, E. Helfand, and P. C. Hohenberg, Physical Review **147,** 295 (1966).

[38] J. W. Yeh, S. K. Chen, S. J. Lin, J. Y. Gan, T. S. Chin, T. T. Shun, C. H. Tsau, and S. Y. Chang, Advanced Engineering Materials **6,** 299 (2004).

[39] B. Cantor, I. T. H. Chang, P. Knight, and A. J. B. Vincent, Materials Science and Engineering: A **375-377,** 213 (2004).

[40] J. J. Hamlin, Physica C: Superconductivity and its Applications **514,** 59 (2015).

[41] K. Jasiewicz, B. Wiendlocha, K. Górnicka, K. Gofryk, M. Gazda, T. Klimczuk, and J. Tobola, Physical Review B **100** (2019).

[42] P. B. Allen and R. C. Dynes, Physical Review B **12,** 905 (1975).

[43] M. R. Kasem, Y. Nakahira, H. Yamaoka, R. Matsumoto, A. Yamashita, H. Ishii, N. Hiraoka, Y. Takano, Y. Goto, and Y. Mizuguchi, Scientific Reports **12** (2022).

[44] L. Zeng, Z. Wang, J. Song, G. Lin, R. Guo, S. C. Luo, S. Guo, K. Li, P. Yu, C. Zhang, W. M. Guo, J. Ma, Y. Hou, and H. Luo, Advanced Functional Materials **33** (2023).

[45] L. Zeng, X. Hu, Y. Zhou, M. Boubeche, R. Guo, Y. Liu, S. C. Luo, S. Guo, K. Li, P. Yu, C. Zhang, W. M. Guo, L. Sun, D. X. Yao, and H. Luo, Adv Sci (Weinh) **11,** e2305054 (2024).

[46] R. Sereika, S. Iwan, P. A. Baker, W. Bi, and Y. K. Vohra, AIP Advances **14** (2024).

[47] L. Wu, J. Si, S. Guan, H. Zhang, J. Dou, J. Luo, J. Yang, H. Yu, J. Zhang, X. Ma, P. Yang, R. Zhou, M. Liu, F. Hong, and X. Yu, Phys Rev Lett **132,** 166002 (2024).

[48] H. Hisazawa, Y. Terada, F. Adziman, D. Crudden, D. Collins, D. Armstrong, and R. Reed, Metals **7,** 71 (2017).

[49] D. Larbalestier, A. Gurevich, D. M. Feldmann, and A. Polyanskii, Nature **414,** 368 (2001).

[50] Y.-F. Kao, T.-J. Chen, S.-K. Chen, and J.-W. Yeh, Journal of Alloys and Compounds **488,** 57 (2009).

[51] N. D. Stepanov, D. G. Shaysultanov, G. A. Salishchev, M. A. Tikhonovsky, E. E. Oleynik, A. S. Tortika, and O. N. Senkov, Journal of Alloys and Compounds **628,** 170 (2015).

[52] W. Yang, S. Pang, Y. Liu, Q. Wang, P. K. Liaw, and T. Zhang, Intermetallics **141,** 107421 (2022).

[53] X.-W. Qiu, Journal of Alloys and Compounds **555,** 246 (2013).

[54] S. Fang, W. Chen, and Z. Fu, Materials & Design (1980-2015) **54,** 973 (2014).

[55] W. Chen, Z. Fu, S. Fang, H. Xiao, and D. Zhu, Materials & Design **51,** 854 (2013).

[56] Y. Dong, K. Zhou, Y. Lu, X. Gao, T. Wang, and T. Li, Materials & Design **57,** 67 (2014).

[57] C. Wang, W. Ji, and Z. Fu, Advanced Powder Technology **25,** 1334 (2014).

[58] W. Chen, Z. Fu, S. Fang, Y. Wang, H. Xiao, and D. Zhu, Materials Science and Engineering: A **565,** 439 (2013).

[59] K. Chakrabarty, A. D. Pope, A. Yadav, W. Yang, J. Ren, V. Rangari, W. Chen, and Y. K. Vohra, Journal of Alloys and Compounds **1020,** 179470 (2025).

[60] S. G. Ma and Y. Zhang, Materials Science and Engineering: A **532,** 480 (2012).

[61] S. Varalakshmi, M. Kamaraj, and B. S. Murty, Metallurgical and Materials Transactions A **41,** 2703 (2010).

[62] D. Stork, P. Agostini, J. L. Boutard, D. Buckthorpe, E. Diegele, S. L. Dudarev, C. English, G. Federici, M. R. Gilbert, S. Gonzalez, A. Ibarra, C. Linsmeier, A. Li Puma, G. Marbach, P. F. Morris, L. W. Packer, B. Raj, M. Rieth, M. Q. Tran, D. J. Ward, and S. J. Zinkle, Journal of Nuclear Materials **455,** 277 (2014).